Progress In Electromagnetics Research, Vol. 165, 47–65, 2019

On the Solution of Inverse Equivalent Surface-Source Problems

Jonas Kornprobst*, Raimund A. M. Mauermayer, Ole Neitz, Josef Knapp, and Thomas F. Eibert

Abstract—Various formulations of the inverse equivalent surface-source problem and corresponding solution approaches are discussed and investigated. Starting from the radiation integrals of electric and magnetic surface current densities, the probe-corrected inverse equivalent source formulation is set up together with different forms of side constraints such as the zero-field or Love condition. The linear systems of equations resulting from the discretized forms of these equations are solved by the normal residual (NR) and normal error (NE) systems of equations. As expected and as demonstrated by the solution of a variety of inverse equivalent surface-source problems, related to synthetic as well as realistic antenna near-field measurement data, it is found that the iterative solution of the NE equations allows for a better control of the solution error and leads in general to a slightly faster convergence. Moreover, the results show that the incorporation of the zero-field condition into the solution process is in general not beneficial, which is also supported by the structure of the NE systems of equations. If desired, Love surface current densities, or just fields in general, can more easily be computed in a post-processing step. The accuracy of the obtained near-fields and far-fields depends more on the stopping criterion of the inverse source solver than on the particular choice of the equivalent surface-source representation, where the zero-field condition may influence the stopping criterion in a rather unpredictable way.

1. INTRODUCTION

Inverse equivalent source solvers have become very mature tools for the flexible and efficient transformation of antenna fields, in particular of measured near-fields (NFs) [1], over the past 25 years. Since surface-source representations are sufficient and efficient for time-harmonic fields, we focus in this paper on such formulations only. Early formulations worked with planar surface current densities together with planar NF scanning surfaces [2, 3], where only one type of surface current density, e.g., the magnetic surface current density, was involved. A rather general three-dimensional formulation with electric and magnetic surface current densities was presented in [4]. Based on the observation that a formulation with electric and magnetic surface current densities (sometimes also called dual-source formulation) is redundant, dual-equation formulations were introduced and discussed in [5–9] that work with a zero-field or Love condition for the fields in order to eliminate the redundancy of the dual-source approach. Zero-field condition means here that the fields due to the sources on a closed Huygens surface around the antenna under test (AUT) are forced to be zero within the enclosed volume. The surface currents obtained under the zero-field condition have a direct relation to the tangential components of the electric and magnetic fields and support thus physical intuition towards the diagnostic interpretation of the obtained results. The question remains, however, whether these Love currents can be computed from "other valid surface sources" in a post-processing step with the same or an even better quality (see also [5]). A clear downside of the zero-field condition is its considerable numerical extra effort,

Received 9 May 2019, Accepted 11 July 2019, Scheduled 2 August 2019
* Corresponding author: Jonas Kornprobst (j.kornprobst@tum.de).
The authors are with the Chair of High-Frequency Engineering, Department of Electrical and Computer Engineering, Technical University of Munich, Munich 80290, Germany.

which can easily exceed the effort required for the solution of the actual inverse equivalent surface-source problem (IESSP) without additional constraint. Instead of working with electric and magnetic surface current densities at the same time, it is also possible to work with just one of these surface current types [5, 6, 10], where the corresponding integral operators are, however, not advantageous for a solution with an iterative solver. As an approximation of the zero-field condition, the combined-source condition has been proposed in [11] in strong-form, with basis functions in form of the well-known Huygens elementary radiators, and in weak form in [12]. Interesting to mention is also the work described in [13–15], where the focus was on radome applications and where the body-of-revolution symmetry was utilized in order to decompose the inverse equivalent current problem by the corresponding eigenmodes. The techniques in [16, 17] work with full matrix representations of the transformation problem and are, thus, very flexible in terms of measurement sample locations, but they are not accelerated, and by working with modal expansions they do not directly have diagnostics capabilities.

Since the IESSPs are in general either over-determined (i.e., more measurement samples than unknowns) or (in most cases) under-determined (i.e., less measurement samples than unknowns), they are commonly solved in a least mean square sense by an iterative solver working on a normal system of equations [18] or by singular value decomposition (e.g., in [19]), where the option with an iterative solver appears to be more or less mandatory for large problems with millions of unknowns or even more. Interesting to note is here that all published IESSP solvers work with the normal residual (NR) system of normal equations, in so far this is evident from the available literature. In [20–22], the NR normal system of equations is explicitly formed and then solved by the generalized minimal residual solver (GMRES) [18], in [2] the NR system of normal equations is solved by the conjugate gradient normal residual (CGNR) solver and the same approach is followed in [4]. In [5, 6], very detailed investigations on solution errors are presented, as well as singular value spectra, again on the basis of the NR system of normal equations. The NR type of equations are utilized in [7, 8], too, together with a Tikhonov-based formulation, where the weighting coefficient for the Love-condition constraint equations is obtained by evaluating the L-curve.

Very important for large IESSPs is to work with an acceleration approach, which helps to handle the fully-populated matrices resulting from the discretization of the integral operators. Most appropriate appear here approaches following the principles of the fast multipole method (FMM) [23–25] or even of the multilevel fast multipole method (MLFMM) [11, 20, 26, 27]. Algebraic compression schemes such as the adpative cross approximation (ACA) method can of course also be employed [28–30].

The major goal of this work is to introduce IESSP formulations and iterative solutions, which provide for improved control of the solution process. Reviewing the available literature, information about the stopping criteria of the iterative solver is rarely found and the given residual errors, in case they are provided, are rather meaningless. A certain residual error level, which gives good results for one problem or IESSP formulation, can lead to considerably worse results in another situation. When working with the NR system of normal equations, the actual error with respect to the field observations or measurement values, called observation error (OE) in the following, can already start to become unstable before the iterative solver residual starts to stagnate. This issue is overcome by working with the normal error (NE) system of normal equations [18], which is commonly recommended for under-determined systems of equations. Instead of working on a more or less meaningless residual error, the NE system of equations works directly on the OE in case of an IESSP and gives, therefore, direct control of the OE. The actual unknowns of the NE system of equations are in the space of the observation samples and in this sense, the NE system of equations realizes the up-sampling scheme as advised in [31], at least in part. It is found that an iterative solution of an NE system of equations stops reliably when the achievable OE has been reached within the given tolerance. As a byproduct, it is observed that the iterative solver convergence is also slightly better than in the case of the corresponding NR system of normal equations.

A variety of IESSP formulations with different equivalent surface-source representations is evaluated based on its NE systems of equations and compared to the corresponding solutions with NR systems of equations. The different formulations comprise single-source equations and dual-source equations, the latter with and without several kinds of additional constraints. In particular, we investigate also a zero-field condition in form of Calderón projections [32, 33], which has the great advantage that it does not require a problem-specific weighting of the constraint equations.

The paper is organized as follows. First, the considered field transformation configuration is explained, and the IESSP transmission together with the optional constraint equations are introduced and discussed. Next, the relevant operator equations are discretized and the NR and NE systems of normal equations are introduced and adapted to all the relevant formulations. In the results section, an extensive study of the solution behavior of the various solver and formulation choices is performed, where one synthetic measurement scenario with simulated field data and one realistic measurement scenario with real spherical NF measurements is considered. Finally, the observed results are evaluated and conclusions are drawn.

2. INVERSE EQUIVALENT SURFACE-SOURCE SOLUTION

2.1. Field Transformation Configuration and Basic Equations

Consider an inverse equivalent surface-source formulation as depicted in Fig. 1. Equivalent electric and magnetic surface current densities $\mathbf{J}_A$ and $\mathbf{M}_A$ are introduced on a closed surface A around the test volume containing all radiation sources of the AUT. The equivalent surface sources are unknown quantities, which shall be determined in a way that they produce the AUT radiation fields in form of the measurement samples $U(\mathbf{r}_m)$ on the measurement surface S, which is in general located in some (arbitrary) distance away from A — typically in the near field of the AUT — and also closed[†]. Following the notation in [11, 22], the probe-weighted radiation integral of the equivalent surface current densities can be written in the form

$$U(\mathbf{r}_m) = \iiint_{V_w} \mathbf{w}(\mathbf{r}-\mathbf{r}_m) \cdot \iint_A \left[\bar{\mathbf{G}}_J^E(\mathbf{r},\mathbf{r}') \cdot \mathbf{J}_A(\mathbf{r}') + \bar{\mathbf{G}}_M^E(\mathbf{r},\mathbf{r}') \cdot \mathbf{M}_A(\mathbf{r}')\right] \mathrm{d}a' \, \mathrm{d}v, \tag{1}$$

where a suppressed time factor $\mathrm{e}^{j\omega t}$ dependent on the angular frequency ω is assumed for all fields and sources. The vector $\mathbf{r}'$ defines source locations, $\mathbf{r}$ observation locations, and $\mathbf{w}$ is a localized function, which produces a weighted field observation in form of the signal (voltage) $U(\mathbf{r}_m)$ at the output of the measurement probe with volume V_w at location $\mathbf{r}_m$. This testing function $\mathbf{w}$ represents a volumetric electric current density which is an equivalent representation of the probe antenna: The far-field radiation characteristic of the probe antenna must be identical to the far field of the equivalent current density $\mathbf{w}$. In a practical implementation with MLFMM-acceleration it is of course more convenient to work with plane-wave spectra. The Green's functions $\bar{\mathbf{G}}_J^E$ and $\bar{\mathbf{G}}_M^E$, respectively, are

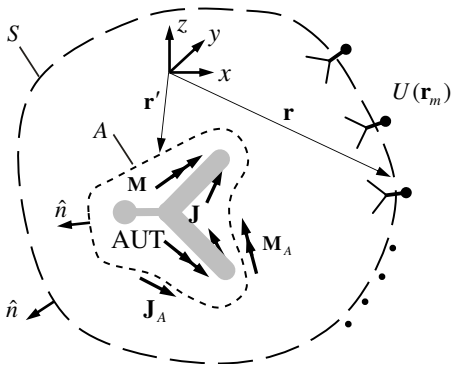

Figure 1. Inverse equivalent source configuration with electric and magnetic surface current densities on a Huygens surface A with outward unit normal $\hat{n}$ and field observations $U(\mathbf{r}_m)$ collected on a closed measurement surface S. The infinite volume outside A is called the solution domain and the surface sources on the surface A are equivalent sources representing the radiation fields of all sources within the enclosed AUT volume.

[†] In practical configurations, the measurement surface S can of course be chosen as an open surface, if possible truncation effects are acceptable. Also, the Huygens surface A can easily be chosen as an open surface as long as the equivalent sources are able to reproduce the observation fields with good enough accuracy.

chosen as Green's functions of free-space in order to simplify the formulation [11, 22, 34]. If desired, the formulation can, however, also be extended towards the consideration of other solution environments, such as for measurements above a metallic ground plane [35] or for measurements above a dielectric ground half-space [36, 37].

The formulation of the forward transmission equation from the sources to the measurement probe given in Equation (1) is a spatial-domain formulation, which is in this form not very convenient for efficient numerical evaluation. A series of other, spectral formulations based on propagating plane waves, possibly in multi-level representation, or in terms of measured scattering parameters instead of probe voltages, are found in a collection of references, such as [11, 20–22, 38].

Due to the uniqueness theorem and the various forms of the Huygens and equivalence principles [5, 11, 34, 39, 40] together with the fact that all original sources are enclosed by the surface A, the following statements about the IESSP hold true:

- Once equivalent surface sources have been found that are able to exactly reproduce the tangential components of the electric and/or magnetic fields on the measurement surface S, represented by the measurement samples $U(\mathbf{r}_m)$, these sources will produce the correct AUT radiation fields everywhere outside of A, no matter whether the surface A is convex or concave.
- Equivalent volume-source distributions in the AUT volume can serve the same purpose, but will not further be considered in the following due to their more complicated placement and control.
- An IESSP formulation with electric and magnetic surface sources is redundant, one type of sources, or a linear combination of the different types of sources, can be used to achieve a unique set of sources. In theory, all the source types can exactly reproduce the observation fields including radiating and evanescent modes. The redundancy among the different sources can be expressed by the superposition of non-radiating surface sources. The justification for the use of different surface source types follows the equivalence principle, as shortly summarized in Appendix A.
- A particular linear combination of the electric and magnetic surface current densities is obtained by enforcing the zero-field or Love condition for all observation locations within the AUT volume[‡]. In this case, the surface current densities are related to the electric and magnetic fields according to

$$\mathbf{J}_A^L\left(\mathbf{r}'\right) = \hat{n} \times \mathbf{H}\left(\mathbf{r}'\right), \quad \mathbf{M}_A^L\left(\mathbf{r}'\right) = -\hat{n} \times \mathbf{E}\left(\mathbf{r}'\right), \tag{2}$$

  where $\hat{n}$ is the unit normal vector on the surface A as seen in Fig. 1 and the superscript L indicates Love current densities.

Towards the solution of inverse equivalent surface-source problems, it must be noted that these problems can be ill-posed in several ways [5]:

- First, if we work with a redundant set of sources, then the sources may be super-imposed by non-radiating sources lying in the null-space of the radiation operator and the problem is severely ill-posed.
- Second, evanescent fields produced by the sources may decay so quickly that they cannot reliably be measured at the surface S or they may be so small in magnitude that their reconstruction may not be possible within the realizable accuracy of the inverse source solution. In this sense, the problem is called mildly ill-posed.
- Third, in practical problem configurations the measurement data is in general super-imposed with noise and/or parasitic signal contributions due to the imperfect measurement environment.

Therefore, it is in general agreed on that the solution of IESSPs requires a solver with certain additional regularization constraints, e.g., related to the smoothness of the solution or related to the energy content of the solution. The null-space due to the redundant field representation with electric and magnetic surface current densities is often removed by additional side constraints, such as the zero-field condition [5, 7, 9, 39] or by a combined-source condition [11, 12]. The option of just working with electric or magnetic surface current densities alone, is commonly not pursued, since the corresponding expansion bases exhibit strong linear interdependencies for 3D problems and the resulting equations are hard to solve by iterative equation solvers. For problems with open measurement surfaces such as a plane, as,

[‡] Due to the uniqueness theorem an enforcement of the zero-field condition on the surface A just inside the AUT volume is sufficient.

e.g., considered in the early days of inverse source solutions [2, 3], electric or magnetic surface current densities alone are, however, a very feasible option.

In order to arrive at the zero-field or Love condition, we can evaluate our weighted radiation integral in Equation (1) directly on the surface A, with a surface vector weighting function $\mathbf{w}_A$, e.g., a typical MoM testing function, instead of the probe weighting function $\mathbf{w}$, resulting in

$$\begin{aligned}\iint_A \mathbf{w}_A(\mathbf{r}) \cdot \mathbf{E}(\mathbf{r})\,\mathrm{d}a \;=\; & \frac{1}{2}\iint_A \mathbf{w}_A(\mathbf{r}) \cdot (\hat{n} \times \mathbf{M}_A(\mathbf{r}))\,\mathrm{d}a \\ & + \iint_A \mathbf{w}_A(\mathbf{r}) \cdot \iint_A \left[\bar{\mathbf{G}}_J^E\left(\mathbf{r},\mathbf{r}'\right) \cdot \mathbf{J}_A\left(\mathbf{r}'\right) + \bar{\mathbf{G}}_M^E\left(\mathbf{r},\mathbf{r}'\right) \cdot \mathbf{M}_A\left(\mathbf{r}'\right)\right] \mathrm{d}a'\,\mathrm{d}a, \quad (3)\end{aligned}$$

where the integral contribution with the factor $\frac{1}{2}$ in front of it comes due to the integration of the singularity of the Green's functions, so that all surface integrals are now defined in a Cauchy principal value sense. With Equation (2) and some vector algebraic arrangements, this equation can be written as

$$\begin{aligned}\iint_A \mathbf{v}_A(\mathbf{r}) \cdot \mathbf{M}_A^L(\mathbf{r})\,\mathrm{d}a \;=\; & \frac{1}{2}\iint_A \mathbf{v}_A(\mathbf{r}) \cdot \mathbf{M}_A(\mathbf{r})\,\mathrm{d}a \\ & - \iint_A \mathbf{w}_A(\mathbf{r}) \cdot \iint_A \left[\bar{\mathbf{G}}_J^E\left(\mathbf{r},\mathbf{r}'\right) \cdot \mathbf{J}_A\left(\mathbf{r}'\right) + \bar{\mathbf{G}}_M^E\left(\mathbf{r},\mathbf{r}'\right) \cdot \mathbf{M}_A\left(\mathbf{r}'\right)\right] \mathrm{d}a'\,\mathrm{d}a, \quad (4)\end{aligned}$$

with $\mathbf{v}_A(\mathbf{r}) = (\hat{n} \times \mathbf{w}_A(\mathbf{r}))$.
A similar equation can be written for the magnetic field, which is given by

$$\begin{aligned}\iint_A \mathbf{v}_A(\mathbf{r}) \cdot Z\mathbf{J}_A^L(\mathbf{r})\,\mathrm{d}a \;=\; & \frac{1}{2}\iint_A \mathbf{v}_A(\mathbf{r}) \cdot Z\mathbf{J}_A(\mathbf{r})\,\mathrm{d}a \\ & + \iint_A \mathbf{w}_A(\mathbf{r}) \cdot Z \iint_A \left[\bar{\mathbf{G}}_J^H\left(\mathbf{r},\mathbf{r}'\right) \cdot \mathbf{J}_A\left(\mathbf{r}'\right) + \bar{\mathbf{G}}_M^H\left(\mathbf{r},\mathbf{r}'\right) \cdot \mathbf{M}_A\left(\mathbf{r}'\right)\right] \mathrm{d}a'\mathrm{d}a \quad (5)\end{aligned}$$

where the characteristic impedance of free space $Z = \sqrt{\mu/\varepsilon}$ with permittivity ε and permeability μ was introduced in order to scale the magnetic field on the same order of magnitude as the electric field. Obviously, these two equations (here written in weighted form) allow to compute Love surface current densities, fulfilling the zero-field condition, from any other surface current densities. In literature, such equations are often denoted as Calderón projections [32, 33].

Enforcing the Love condition as a side constraint can be achieved by replacing the arbitrary surface current densities on the right-hand sides of Equations (4) and (5) by the corresponding Love surface current densities resulting in

$$\frac{1}{2}\iint_A \mathbf{v}_A(\mathbf{r}) \cdot \mathbf{M}_A^L(\mathbf{r})\,\mathrm{d}a = -\iint_A \mathbf{w}_A(\mathbf{r}) \cdot \iint_A \left[\bar{\mathbf{G}}_J^E\left(\mathbf{r},\mathbf{r}'\right) \cdot \mathbf{J}_A^L\left(\mathbf{r}'\right) + \bar{\mathbf{G}}_M^E\left(\mathbf{r},\mathbf{r}'\right) \cdot \mathbf{M}_A^L\left(\mathbf{r}'\right)\right] \mathrm{d}a'\,\mathrm{d}a, \quad (6)$$

and

$$\frac{1}{2}\iint_A \mathbf{v}_A(\mathbf{r}) \cdot Z\mathbf{J}_A^L(\mathbf{r})\,\mathrm{d}a = \iint_A \mathbf{w}_A(\mathbf{r}) \cdot Z \iint_A \left[\bar{\mathbf{G}}_J^H\left(\mathbf{r},\mathbf{r}'\right) \cdot \mathbf{J}_A^L\left(\mathbf{r}'\right) + \bar{\mathbf{G}}_M^H\left(\mathbf{r},\mathbf{r}'\right) \cdot \mathbf{M}_A^L\left(\mathbf{r}'\right)\right] \mathrm{d}a'\,\mathrm{d}a \quad (7)$$

which are nothing else than electric field and magnetic field surface integral equations (EFIE and MFIE), as known from radiation and scattering problems [41], but without incident fields. If desired, the EFIE and the MFIE can be combined into a combined field integral equation (CFIE) in the form of

$$(1-\gamma)\,(\hat{n} \times \mathrm{MFIE}) - \gamma\,\mathrm{EFIE} = 0 \quad (8)$$

where γ is the common CFIE combination parameter, chosen between 0 to 1.
As an approximation of the CFIE, we may write it with the assumption that all integrals on the right-hand side of Equations (6) and (7) are zero and this gives the combined-source (CS) condition [11, 12, 42]

$$\iint_A \left[\mathbf{v}_A(\mathbf{r}) \cdot Z\,(\hat{n} \times \mathbf{J}_A(\mathbf{r})) - \mathbf{M}_A(\mathbf{r})\right] \mathrm{d}a = 0 \quad (9)$$

where γ was here set to 1/2. Also, the superscript L was dropped since we cannot expect Love current densities anymore with this condition.

2.2. Discretization and Solution

Towards the solution of the IESSP, we discretize the electric and magnetic surface current densities by low-order Rao-Wilton-Glisson (RWG) basis functions $\boldsymbol{\beta}$ [43] according to

$$\mathbf{J}_A\left(\mathbf{r}'\right) = \sum_p J_p \boldsymbol{\beta}_p\left(\mathbf{r}'\right) \qquad \mathbf{M}_A\left(\mathbf{r}'\right) = \sum_q M_q \boldsymbol{\beta}_q\left(\mathbf{r}'\right), \tag{10}$$

with $p = 1, ..., P$ and $q = 1, ..., Q$, where, however, higher-order basis functions may also be used [21]. Plugging these expansions into the transmission Equation (1) gives a linear system of equations

$$[L_{mp}]\,[ZJ_p] + [K_{mq}]\,[M_q] = [U_m] \tag{11}$$

with $m = 1, ..., M$, where [.] denotes a discrete vector for an entry with single subscript and a matrix for an entry with double subscript. The matrix elements are given by

$$L_{mp} = \iiint_{V_w} \mathbf{w}\left(\mathbf{r} - \mathbf{r}_m\right) \cdot \iint_A \bar{\mathbf{G}}_J^E\left(\mathbf{r}, \mathbf{r}'\right) \cdot \frac{\boldsymbol{\beta}\left(\mathbf{r}'\right)}{Z}\, \mathrm{d}a'\, \mathrm{d}v \tag{12}$$

$$K_{mp} = \iiint_{V_w} \mathbf{w}\left(\mathbf{r} - \mathbf{r}_m\right) \cdot \iint_A \bar{\mathbf{G}}_M^E\left(\mathbf{r}, \mathbf{r}'\right) \cdot \boldsymbol{\beta}\left(\mathbf{r}'\right)\, \mathrm{d}a'\, \mathrm{d}v \tag{13}$$

and $U_m = U(\mathbf{r}_m)$. Instead of the unknown coefficients J_p, we work with ZJ_p to scale the different surface current types to the same order of magnitude and obtain thus a better conditioned system of equations.

For the discretization of the projection Equations (5) and (4), we choose $\mathbf{v}_A = \boldsymbol{\beta}$ and, thus, $\mathbf{w}_A = -\hat{n} \times \boldsymbol{\beta}$ in order to obtain a well-conditioned Gram matrix on the left-hand side of the equations, resulting in

$$\frac{1}{2}\,[G_{sp}]\left[ZJ_p^L\right] = \left[D_{sp}^J\right][ZJ_p] + \left[B_{sq}^M\right][M_q] \tag{14}$$

$$\frac{1}{2}\,[G_{tp}]\left[M_p^L\right] = \left[B_{tp}^J\right][ZJ_p] + \left[D_{tq}^M\right][M_q] \tag{15}$$

with $s = 1, ..., S$, $t = 1, ..., T$ and p, q as defined before, in most cases with $S = T = P = Q$. The elements of the RWG functions Gram matrix are computed via

$$G_{sp} = \iint_A \boldsymbol{\beta}_s(\mathbf{r}) \cdot \boldsymbol{\beta}_p\left(\mathbf{r}'\right) \mathrm{d}a' \mathrm{d}a. \tag{16}$$

The matrix elements $B_{sp}^{J/M}, D_{sp}^{J/M}$ are easily constructed similar to the expressions in Equations (12), (13), and (16). By inverting the Gram matrices on the left-hand side of the equations in (14) and (15), we obtain the discrete projection equations

$$\begin{aligned}\left[ZJ_p^L\right] &= 2\,[G_{sp}]^{-1}\left(\left[D_{sp}^J\right][ZJ_p] + \left[B_{sq}^M\right][M_q]\right) \\ &= \left[D_{sp}^{'J}\right][ZJ_p] + \left[B_{sq}^{'M}\right][M_q]\end{aligned} \tag{17}$$

$$\begin{aligned}\left[M_p^L\right] &= 2\,[G_{tp}]^{-1}\left(\left[B_{tp}^J\right][ZJ_p] + \left[D_{tq}^M\right][M_q]\right) \\ &= \left[B_{tp}^{'J}\right][ZJ_p] + \left[D_{tq}^{'M}\right][M_q]\end{aligned} \tag{18}$$

to directly compute the unknown electric and magnetic current coefficients with Love constraint from any unconstrained coefficients. In a numerical implementation, these equations suffer from similar accuracy problems as classical MFIE solutions based on RWG functions [44].

In order to discretize the Love-condition side constraint Equations (6) and (7), we choose $\mathbf{w}_A = \boldsymbol{\beta}$ and, thus, $\mathbf{v}_A = \hat{n} \times \boldsymbol{\beta}$, which results in the discrete Love-constraint equations

$$\left[L_{tp}^L\right][ZJ_p] + \left[K_{tq}^L\right][M_q] = 0 \tag{19}$$

$$\left[K_{sp}^{'L}\right][ZJ_p] + \left[L_{sq}^{'L}\right][M_q] = 0 \tag{20}$$

with s, t, p, q as defined before. Also, it is noted that L superscripts of the unknown coefficients have been dropped, but L superscripts for the matrix elements have been introduced. Both of these equations are tested as the classical EFIE, where the matrix elements can formally be written as done for the previous discrete equations.

Finally, the Love constraint in form of the CFIE in Equation (8) can be discretized in a similar way, where the MFIE part would then be tested in a $\hat{n}\times$-rotated form. In the following, the CFIE is not further considered since it is not really beneficial for the solution of our IESSP. The CS condition in (9) can be considered in strong form as shown in [11] or in weak form as found in [12].

Since the inverse equivalent surface-source problem according to Equation (11) has in general more unknown coefficients than equations, it is commonly solved in a least mean square sense in form of the normal system of equations

$$\begin{bmatrix} L_{pm}^* \\ K_{qm}^* \end{bmatrix} \begin{bmatrix} L_{mp} & K_{mq} \end{bmatrix} \begin{bmatrix} ZJ_p \\ M_q \end{bmatrix} = \begin{bmatrix} L_{pm}^* \\ K_{qm}^* \end{bmatrix} [U_m] \tag{21}$$

where * indicates the complex conjugation, and the flipping of the subscripts means the transpose of the corresponding matrix blocks. According to [18], such a system of equations is called a normal residual (NR) system of normal equations. When solved by an iterative solver such as the generalized minimal residual solver (GMRES), which is exclusively considered in this work, due to its good regularization properties (minimization of energy content of solution), this residual error is minimized in the space of the solution vector with commonly more elements than equations. Once the solution vector has been obtained by solving the NR system of equations, the error with respect to the measurement or observation values (OE)

$$\varepsilon_{OE} = \frac{\left| \begin{bmatrix} L_{mp} & K_{mq} \end{bmatrix} \begin{bmatrix} ZJ_p \\ M_q \end{bmatrix} - [U_m] \right|}{|[U_m]|} \tag{22}$$

according to the original equation system in Equation (11) can also be computed.

By introducing the mapping

$$\begin{bmatrix} ZJ_p \\ M_q \end{bmatrix} = \begin{bmatrix} L_{pm}^* \\ K_{qm}^* \end{bmatrix} [u_m] \tag{23}$$

another system of normal equations can be written as

$$\begin{bmatrix} L_{mp} & K_{mq} \end{bmatrix} \begin{bmatrix} L_{pm}^* \\ K_{qm}^* \end{bmatrix} [u_m] = [U_m] \tag{24}$$

which works on the set of unknowns u_m in the space of the NF measurements and has, thus, the same number of unknowns as equations. According to [18], such a system of equations is called a normal error (NE) system of equations and is obviously better suited for under-determined systems of equations as commonly found for our inverse equivalent surface-source problems. The residual error of this NE system of normal equations is identical to the OE of the original equation system.

The discrete Love current projection equations in (17) and (18) can be applied to both systems of normal equations as a pre-conditioner, for the NR system of equations as a left-hand side preconditioner resulting into

$$\begin{bmatrix} D_{sp}^{\prime J} & B_{sq}^{\prime M} \\ B_{tp}^{\prime J} & D_{tq}^{\prime M} \end{bmatrix} \begin{bmatrix} L_{pm}^* \\ K_{qm}^* \end{bmatrix} \begin{bmatrix} L_{mp} & K_{mq} \end{bmatrix} \begin{bmatrix} ZJ_p \\ M_q \end{bmatrix} = \begin{bmatrix} D_{sp}^{\prime J} & B_{sq}^{\prime M} \\ B_{tp}^{\prime J} & D_{tq}^{\prime M} \end{bmatrix} \begin{bmatrix} L_{pm}^* \\ K_{qm}^* \end{bmatrix} [U_m] \tag{25}$$

and for the NE system of normal equations as a kind of right-hand side pre-conditioner leading to

$$\begin{bmatrix} L_{mp} & K_{mq} \end{bmatrix} \begin{bmatrix} D_{sp}^{\prime J} & B_{sq}^{\prime M} \\ B_{tp}^{\prime J} & D_{tq}^{\prime M} \end{bmatrix} \begin{bmatrix} L_{pm}^* \\ K_{qm}^* \end{bmatrix} [u_m] = [U_m] \ . \tag{26}$$

Finally, both systems of normal equations are combined with the Love condition as side constraint equations in (19) and (20). For the NR system of normal equations in (21), we obtain

$$\begin{bmatrix} L_{pm}^* & L_{pt}^{L*} & K_{ps}^{\prime L*} \\ K_{qm}^* & K_{qt}^{L*} & L_{qs}^{\prime L*} \end{bmatrix} \begin{bmatrix} L_{mp} & K_{mq} \\ \lambda L_{tp}^L & \lambda K_{tq}^L \\ \lambda K_{sp}^{\prime L} & \lambda L_{sq}^{\prime L} \end{bmatrix} \begin{bmatrix} ZJ_p \\ M_q \end{bmatrix} = \begin{bmatrix} L_{pm}^* \\ K_{qm}^* \end{bmatrix} [U_m] \tag{27}$$

and for the NE system of normal Equation (24) the result is

$$\begin{bmatrix} L_{mp} & K_{mq} \\ \sqrt{\lambda}L^{L}_{tp} & \sqrt{\lambda}K^{L}_{tq} \\ \sqrt{\lambda}K'^{L}_{sp} & \sqrt{\lambda}L'^{L}_{sq} \end{bmatrix} \begin{bmatrix} L^{*}_{pm} & \sqrt{\lambda}L^{L*}_{pt} & \sqrt{\lambda}K'^{L*}_{ps} \\ K^{*}_{qm} & \sqrt{\lambda}K^{L*}_{qt} & \sqrt{\lambda}L'^{L*}_{qs} \end{bmatrix} \begin{bmatrix} u_m \\ v_t \\ v_s \end{bmatrix} = \begin{bmatrix} U_m \\ 0_t \\ 0_s \end{bmatrix} \tag{28}$$

where v_t and v_s are additional unknowns in the space of the Love condition equations, obtained by a mapping similar to the one in Equation (23).
In both systems of equations, the constant multiplier λ was introduced (in Equation (28) symmetrically as $\sqrt{\lambda}$) in order to allow for an appropriate scaling of the constraint equations with respect to the actual inverse equivalent source equations. The multiplier can be chosen empirically, but its proper value can also be determined from an analysis of the properties of the individual submatrices or by following the L-curve approach [7, 8]. Since the correct choice of this scaling parameter depends strongly on the measurement configuration as well as on the quality of the measurement data (noise level), its need is certainly a disadvantage of the formulations with Love condition in form of a side constraint.

In contrast to radiation and scattering problems of computational electromagnetics [41], where commonly well-determined systems of equations with equal numbers of unknowns and equations are considered, it is here obviously relatively simple to include the constraint equations separately for the electric and magnetic fields and obtain more equations than actually needed. Within the systems of normal equations, everything is solved together in a least mean square sense and there is thus no need to work with a halved number of equations in form of the CFIE.

If the CS condition in Equation (9) shall be considered as a side constraint, then it is recommended to either use it in strong form as in [45] or to invert the involved Gram matrix explicitly whenever the current coefficients are needed within the solution of IESSPs according to Equation (21) or (24). Both of these methods are computationally very efficient and avoid to handle an additional side constraint with the corresponding weighting parameter λ. The option to solve the Love constraint equations explicitly for one type of currents within every iteration is, in contrast, not beneficial, due to the considerably larger computational effort.

As already said before, due to the size of the systems of equations it is recommended to solve them with an iterative linear system of equations solver, where we use GMRES [18] in this work. It is also recommended to support the solution of the systems of equations by utilizing some kind of fast algorithm for the evaluation of the involved matrix-vector products. The most efficient and still accurate algorithms in this respect appear to be hierarchical multi-level algorithms working with a decomposition of the fields into propagating plane waves [11, 22, 26, 27], which may be upgraded by the use of directive Gaussian-beam based translation operators [11, 46].

3. FIELD TRANSFORMATION RESULTS

3.1. Horn Antenna — Synthetic Measurement Data

3.1.1. Synthetic Measurement Generation

The first AUT under consideration is a simulation model of a pyramidal horn antenna with infinitely thin perfectly conducting walls. The NF measurement data and the reference FF patterns have been generated by FEKO using the method of moments solver [47]. The reason for utilizing synthetically generated measurement data is that a highly-accurate solution (i.e., a reference solution) can be obtained from the simulation. Dependent on the accuracy settings in the simulation and in the IESSP solution, reconstruction accuracies can be achieved, which are considerably better than for measurements wich unavoidable uncertainties and noise. The utilized triangular IESSP reconstruction mesh consisting of 6322 triangles as shown in Fig. 2 also gives the geometric dimensions of the AUT. The shown mesh is obviously closed. The mesh for the FEKO simulations was similar, but without the aperture closing, i.e., the FEKO mesh was open. A rectangular waveguide port forms the excitation of the dominant H_{10} mode. The simulations have been carried out for a frequency of $f = 11\,\mathrm{GHz}$, the wavelength at this frequency is $\lambda = 27.3\,\mathrm{mm}$ and the common FF distance according to $r_{FF} = 2D^2_{AUT}/\lambda$ is around $0.7\,\mathrm{m}$, where D_{AUT} is the diameter of the minimum sphere enclosing the AUT.

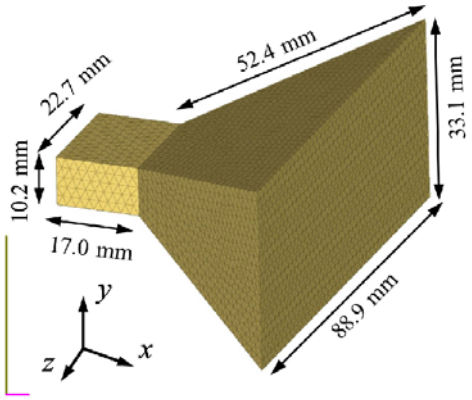

Figure 2. Pyramidal horn antenna mesh with geometric dimensions.

Considered is a spherical measurement configuration with regular sampling in ϑ and φ and a measurement distance of 0.1 m. Synthetic NF data have been computed for 30 sample locations in ϑ and 60 in φ, two orthogonal polarizations for each location. The assumed measurement probe is a Hertzian dipole. The total number of the synthetic measurement values is 3600, where samples at the poles are avoided by starting the sampling in ϑ at 3°.

3.1.2. Transformation Results

The E-plane vertical FF cut of this AUT is depicted in Fig. 3 for different IESSP solver configurations in comparison to the FEKO reference data. The explanation of the acronyms used to denote the different solver configurations is found in Table 1. J NE is obviously a solver working with electric surface current densities only and by iterative solution of the NE system of normal equations. JM NE is the corresponding solver with electric and magnetic surface current densities without additional constraint equations. The shown error or deviation measure for all patterns in this paper is the linear magnitude error normalized to the maximum of the magnitude of the reference pattern. It is quite good for both of the solver configurations, i.e., even for the electric surface currents only, which are known to lead to worse conditioned equation systems than dual-source formulations [5]. All solver configurations as found in Table 1 give here rather similar accuracies and are not worth to be discussed in detail. The

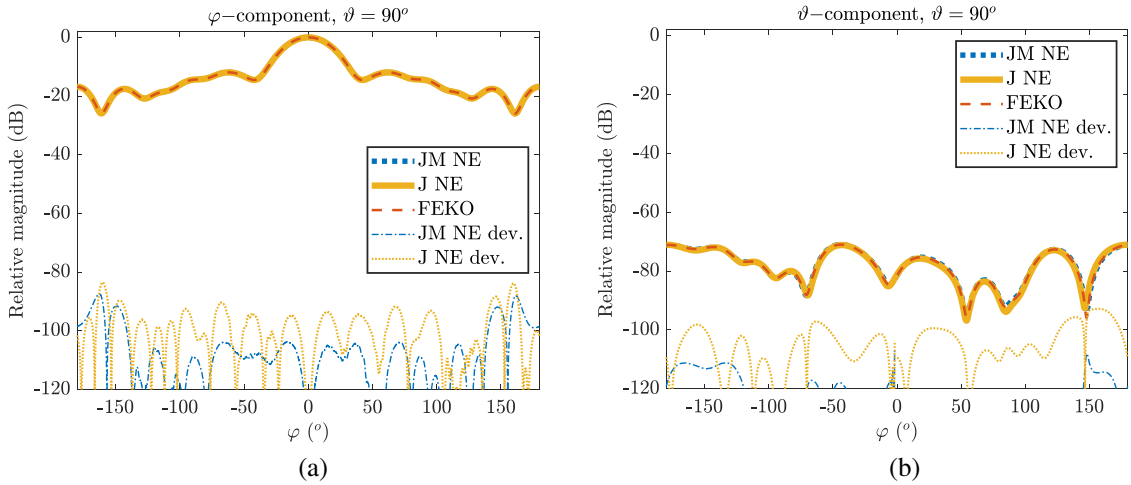

Figure 3. Horizontal far-field pattern cut of the horn antenna as seen in Fig. 2 in comparison to MoM reference results by FEKO [47], see Table 1 for explanation of legends. (a) Co-polarized component. (b) Cross-polarized component.

Table 1. Explanation of acronyms in figure legends.

Acronym	Explanation
J	electric surface currents only
JH	directive Huygens radiators based on electric surface currents, strong form according to (9)
JM	electric and magnetic surface currents, no constraint
JM Love CP	JM, but with Love current projection according to (17) and (18)
JM Love SC	JM, but with Love condition as side constraint according to (19) and (20)
JM WF CS	JM, but with weak-form combined-source condition according to (9)
NR	normal residual system of normal equations
NE	normal error system of normal equations
FEKO	commercial electromagnetics solver [47]
NSI-MI	spherical mode NF FF transformation by NSI-MI [48]
dev.	deviation between an IESSP solution and results from either a reference or another NF FF transformation

necessary computation time for one of these transformations using our multi-level implementation (no additional side constraint such as a zero-field condition) is on the order of half a minute on a standard desktop computer (Intel Core i7-4820K @ 3.70 GHz, four cores).

The solution and iteration behaviour of various solver configurations according to Table 1 is summarized in Fig. 4. The graph in Fig. 4(a) shows the solver residual for NR systems of normal equations and the graph in Fig. 4(b) provides the same results for the corresponding NE systems of normal equations. The NE residual is identical to the OE except for the solution with Love condition as a side constraint, where the residual contains also the contributions due to v_t and v_s as found in Equation (28). In contrast, the NR residual is defined in the space of the solution vector (see Section 2.2). The NE residual, i.e., the OE reaches here a comparable level as the FF error in Fig. 3 and also the NR solvers reach this OE level, see Fig. 4(c), except for the solver with the Love condition in form of the Love current projections. However, it must be noted that the NR residual needs to reach until below $-140\,\mathrm{dB}$ before the OE level of about $-80\,\mathrm{dB}$ is reached. The termination criterion for all solver runs was relative in a way that the solver stopped, when 3 iterations in a row did not give a relative residual improvement of better than 0.9999. All solver choices stopped with this criterion and also all of them needed about the same number of iterations to reach the stopping criterion, where the OE was about the same for all of them, except for the NR solver with the Love current projections. Obviously, the projections introduce additional errors, which limit the achievable OE and thus also the FF error to around $-65\,\mathrm{dB}$ when utilized within the NR system of equations. It is interesting to note that some of the NR solutions without Love constraint show OE oscillations towards the end of the iteration process, which can, however, easily be avoided by stopping the solver early enough[§]. In the NE system of equations, the Love current projections do not show any notable effect. When the Love condition is considered in the form of an additional side constraint, then it is obvious that the convergence behavior of both solver types changes, where, however, still similar values of the residuals are achieved at the end, if the weighting of the Love condition via the scaling parameter is not too strong[‖]. Fig. 4(c) compares

[§] The JM WF CS NR solver (not included in Fig. 4(c)) did also stop early enough by itself.

[‖] As said before, the particular choice of the scaling parameter is problem-specific and can, e.g., be found following the L-curve method [7, 8].

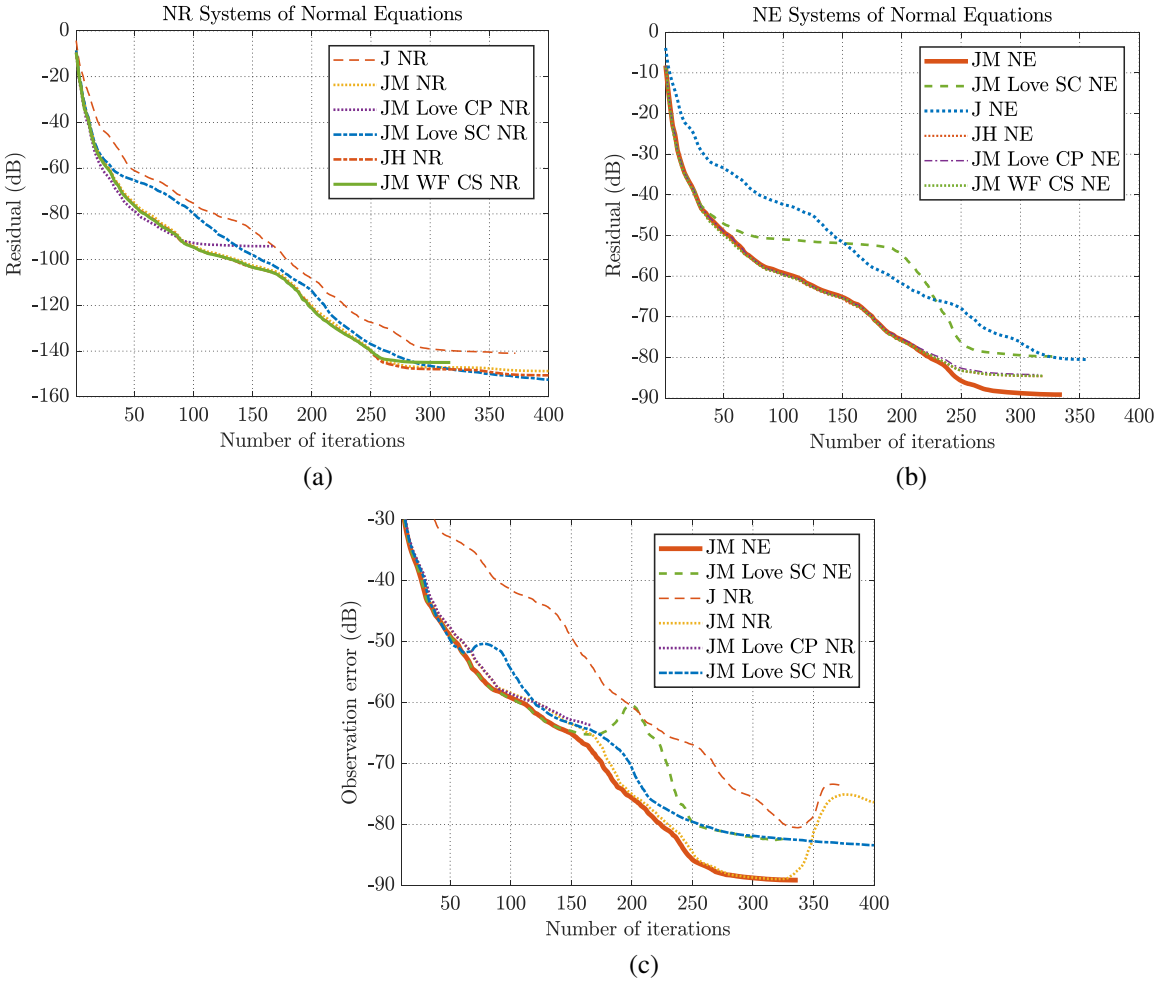

Figure 4. Convergence behavior of different inverse equivalent surface-source solvers for the horn antenna in Fig. 2, for legend explanation see Table 1. Except for JM Love SC NE, the residuals of the NE equations in subfigure (b) are identical to the corresponding observation errors in subfigure (c). (a) Residual of NR equations. (b) Residual of NE equations. (c) Exemplary observation errors of NR and NE equations.

the OEs of both solver types, where it should be noted that in NR solutions the computation of the OE in every iteration is not standard and causes extra computation effort, in particular in an iterative solver such as GMRES. The NE solvers with no or a simple CS side constraint show obviously the best convergence behavior of the OE, where, however, the NR solutions are not much worse, except for the fact that the OE can start to increase and oscillate, if the iterations are not stopped early enough. This behavior is expected to become worse when the measurement data contains imperfections or noise. In both cases, the solvers with Love condition behave worse than the solvers with no or a simple side constraint. For the solutions with Love condition as a side constraint, the convergence behavior depends strongly on the chosen weighting of the side constraint. The given convergence results are for a typical setting of the weighting parameter ($\lambda = 0.1$ in case of NE and $\lambda = 10$ in case of NR). An evaluation of the NF distribution very close to the Huygens surface for JM NE solvers without Love condition and with Love condition in form of a side constraint is illustrated in Fig. 5. Fig. 5(a) is for an IESSP solution working directly on the FEKO NF data, whereas for Fig. 5(b) random noise with a signal-to-noise ratio (SNR) of 40 dB with respect to the maximum of the NF observation data was added. The shown NF difference is the linear magnitude difference with respect to the linear magnitude average

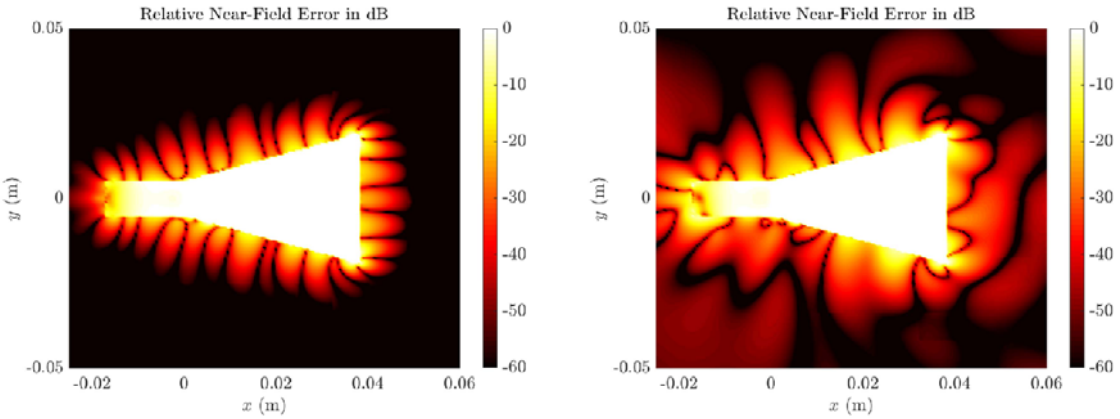

Figure 5. NF magnitude differences between JM NE and JM Love SC NE solutions for NF data with 0.1 m distance for the horn antenna as seen in Fig. 2, see Table 1 for explanation of acroyms. (a) FEKO NF data. (b) FEKO NF data plus noise, SNR = 40 dB.

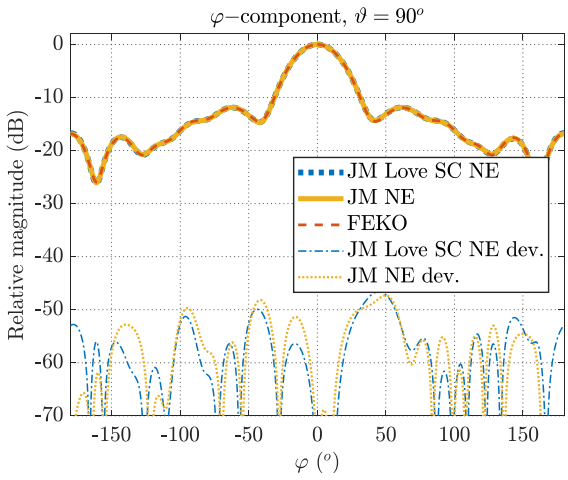

Figure 6. Horizontal far-field pattern cut of the horn antenna as seen in Fig. 2 for noisy NF data (SNR = 40 dB, 0.1 m distance) in comparison to MoM reference results by FEKO [47], see Table 1 for explanation of legends.

over the complete range of one of the solutions. It is clearly seen that the range with somewhat larger differences is very localized around the mesh and if every single solution was compared to the FEKO reference it would not be possible to decide which one is better. Looking into the NF distribution of the JM NR solution, where the OE started already to become unstable, see Fig. 4(c), a larger NF difference with respect to the FEKO data is also observed. Finally, Fig. 6 shows an FF pattern cut obtained from IESSP solutions with noisy NF data. Again, the difference between the JM NE and the JM Love SC NE results is marginal, where, however, the FF pattern accuracy of around −50 dB is about 10 dB better than the SNR of the NF observation data in 0.1 m distance. The OE, as seen in Fig. 5 is for these solutions on the order of −25 dB only, since it is not normalized with respect to the maximum but with respect to the squared average of the observation field data.

In summary, we can say that the simple IESSP solvers without additional side constraint, or with the simple CS condition, show the best behavior for the lowest computational effort and the solution of the NE systems of normal equations allows for a more direct control of the solution accuracy. For the NR systems, it would certainly also be possible to control the convergence dependent on the OE and not dependent on the residual, but this would in general need extra computations within the solver.

3.2. Double-Ridged Waveguide Horn Antenna — Real Measurement Data

3.2.1. Measurement Setup

To evaluate the solution behavior of the different IESSP formulations and solvers with measured NF data, we consider an HF907 double-ridged waveguide horn antenna from Rohde & Schwarz as shown in Fig. 7. The geometric size of the HF907 antenna in x, y, z-direction, respectively, is about $0.280\,\mathrm{m} \times 0.226\,\mathrm{m} \times 0.305\,\mathrm{m}$ ($16.8\lambda \times 13.6\lambda \times 18.3\lambda$); the common FF distance is approximately 17 m. The selected measurement frequency of 18 GHz is at the upper working frequency limit of this ultra-wideband antenna. Spherical measurements with a distance of 2.73 m from the rotation center and with 45 451 measurement locations (two measured polarizations for each), regularly spaced in ϑ and φ, have been performed in the anechoic chamber of the Technical University of Munich. A open-ended rectangular hollow waveguide was utilized as measurement probe.

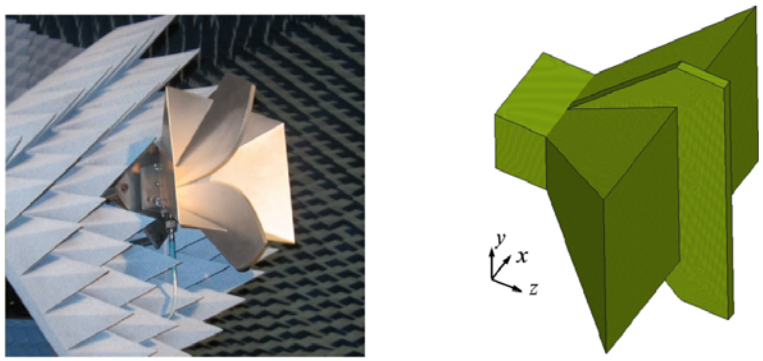

(a) (b)

Figure 7. Double-ridged waveguide horn HF907 by Rohde & Schwarz [49]. (a) Photograph in anechoic chamber. (b) Conformal mesh for field transformations.

3.2.2. Transformation Results

The IESSP solutions have been obtained with sources defined on two different meshes, the conformal mesh seen in Fig. 7(b) with 188 090 triangles and with a spherical mesh tightly enclosing the AUT. The AUT and also the meshes are slightly offset from the rotation center in $-z$-direction, so that the ends of the ridges are close to the rotation center. A summary of the solution and iteration behavior of the different IESSP solver choices is given in Fig. 8 for both meshes. Again, separate plots for the iteration count dependent residuals of the NR and the NE systems of normal equations are given together with a comparison of the corresponding OEs. The explanation of the legends is found in Table 1. The solution times for the JH NE solutions were around 16 min for the conformal mesh and around 10 min for the spherical mesh, respectively, again on a standard desktop computer (Intel Core i7-4820K @ 3.70 GHz, four cores).

The stopping criterion of all solver runs was achieved, when 3 iterations in a row did not yield a relative residual improvement of better than 0.999[¶]. All solver runs stopped with this criterion and all solutions achieved about the same OE level. However, while the NE solutions stopped well-defined, the NR solutions continued far longer until they terminated, which is again a clear indication that the residual of the NR equations is not that directly related to the OE. As expected, the electric currents-only solvers show again the worst convergence behavior. The solvers with Love current projections show rather similar behavior to the JM solvers with no or a simple CS condition, no matter whether in weak or in strong form. Only the NR solution with Love projection stops rather early, which is obviously due to the additional numerical error of the Love projections. The solutions with Love condition as a side constraint show a rather different convergence behavior during the course of the iterations. Due to residuals which now also contain the deviations of the additional side constraints, this is, however, expected. Interesting is again that the residuals and also the OEs reach about the same values as without

[¶] This stopping criterion is more relaxed than for the synthetic example due to the worse achievable OE.

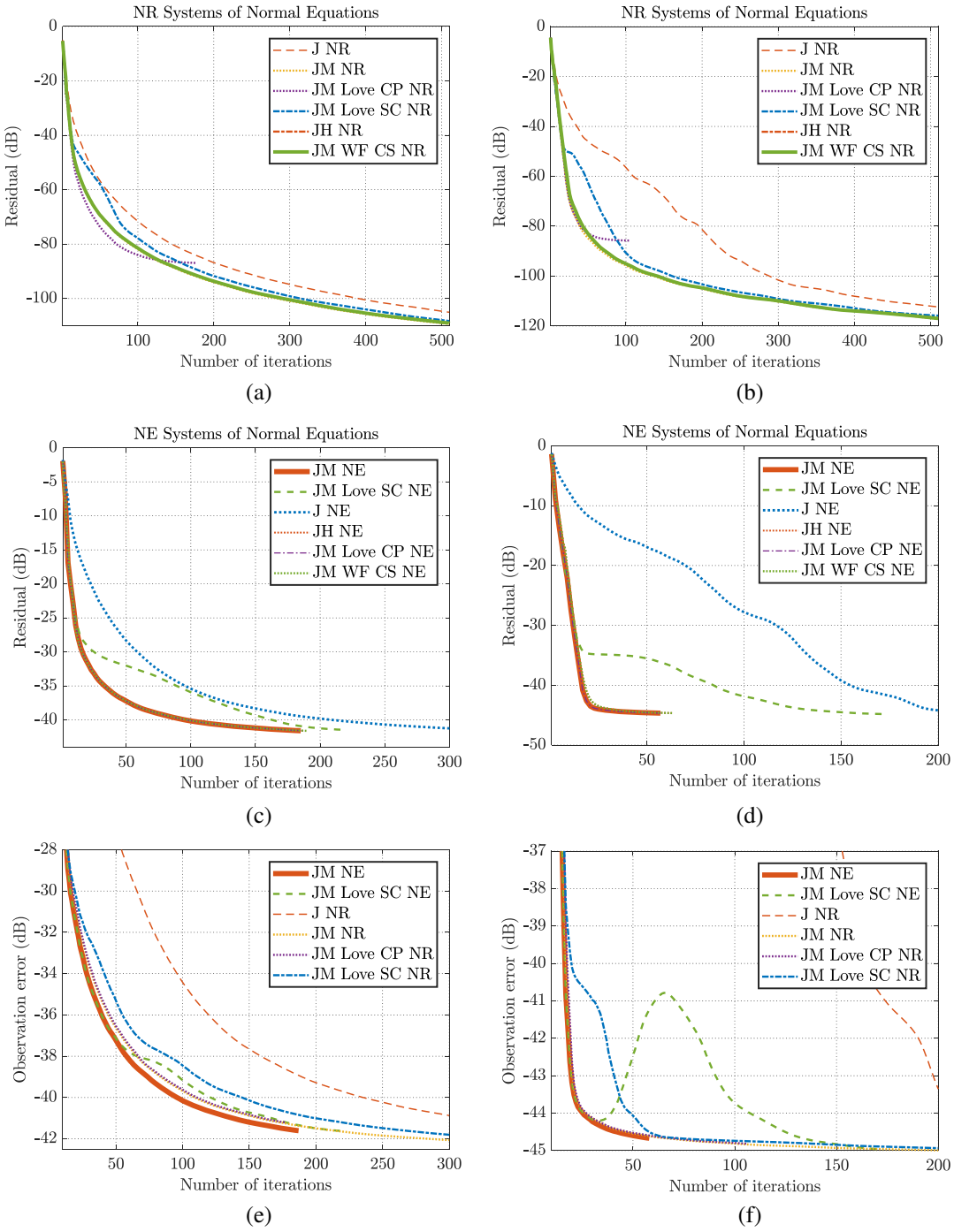

Figure 8. Convergence behavior of different inverse equivalent surface-source solvers for the HF907 antenna in Fig. 7, the left row (a), (c), (e) with the mesh in Fig. 7(b), the right row (b), (d), (f) with a spherical mesh tightly enclosing the antenna. Except for JM Love SC NE, the residuals of the NE equations in subfigure (c) and (d) are identical to the corresponding observation errors in subfigure (e) and (f), respectively. (a) Residual of NR equations. (b) Residual of NR equations. (c) Residual of NE equation. (d) Residual of NE equation. (e) Exemplary observation errors of NR and NE equations. (f) Exemplary observation errors of NR and NE equations.

Love-condition side constraint. Concerning the OE, it is again found that the NE solutions converge slightly faster than the NR solutions. Interesting is also that the OEs achieved with the spherical mesh as seen in Fig. 8 are a few dB lower than for the case of the conformal mesh as found in Fig. 8. This

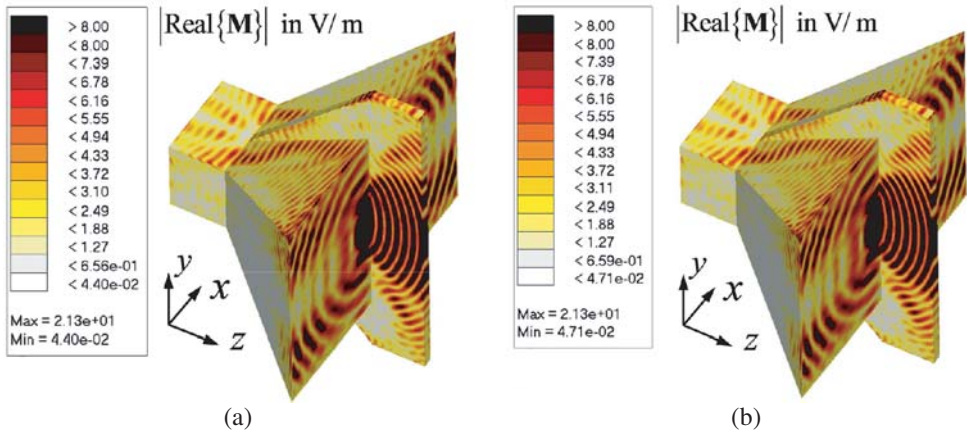

Figure 9. Magnetic Love surface current densities on the conformal mesh in Fig. 7(b) for the HF907 antenna. (a) Result of JM Love NE. (b) Result of JM NE with post-processing.

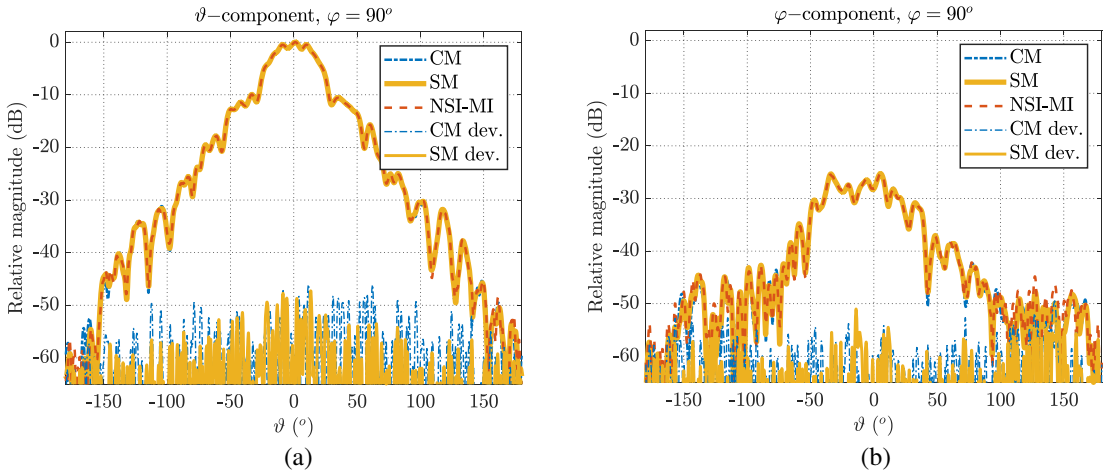

Figure 10. *E*-plane far-field pattern cut of the HF907 antenna as seen in Fig. 7, in comparison to NSI-MI spherical mode expansion based results [48], CM: conformal mesh in Fig. 7(b), SM: tight spherical mesh, both obtained by JM NE, see Table 1. (a) Co-polarized component. (b) Cross-polarized component.

can be explained by the fact that the spatial extent of the spherical mesh is larger and the sources on the spherical mesh are thus able to represent more of the parasitic field contributions coming from the absorber behind the AUT and from the fixtures of the positioner. In contrast, the conformal mesh removes some of the parasitic field contributions by spatial filtering. Overall, it is also observed that the solutions with the spherical mesh converge considerably more quickly than the solutions with the conformal mesh. The well-defined stop of the NE solutions at the achievable OE is remarkable. Again, the NR solutions continue considerably longer before they reach the stopping criterion.

In Fig. 9, two examples of computed surface current distributions are shown. Both are Love currents of the magnetic type corresponding to the tangential electric field. One is obtained from a true solution with Love current projections during the entire iterative solution, the second one is obtained in a post-processing step from an unconstraint solution, again by Love current projection. The differences of both surface current distributions are certainly negligible. Finally, Fig. 10 shows *E*-plane FF cuts of the antenna obtained from IESSP solutions in comparison to pattern values obtained with the spherical-mode based NF FF transformation from NSI-MI [48]. The agreement of the IESSP solution with the spherical mesh is, as expected, somewhat closer to the spherical-mode result, which is obtained with even less pronounced spatial filtering. The achieved deviation of the different patterns is on the order of what can be expected with the available measurement equipment.

4. CONCLUSION

A variety of inverse equivalent surface-source formulations with different kinds of sources and different kinds of additional constraint equations were investigated. The discretized systems of equations were solved in the form of normal systems of equations. In addition to the commonly employed normal residual (NR) systems of normal equations, we considered also the normal error (NE) systems of normal equations, which were found to be a better choice for the iterative solution of inverse equivalent surface-source problems (IESSPs). The NE solutions work directly on the error with respect to the measurements or observations (OE) of the IESSP, which are actually the relevant quantity in the area of antenna field measurements. In contrast, the residual of the NR equations is defined in the commonly considerably larger space of the discrete sources and its relation to the relevant OE is strongly dependent on the particular measurement and transformation configuration. The iterative solutions of the NE systems of normal equations were found to stop reliably when the achievable OE was reached and their convergence behavior with respect to the OE was found to be slightly better compared to NR systems of equations solutions. With respect to additional side constraints such as the Love or zero-field condition, we could not find any evidence that such conditions are beneficial compared to unconstraint solutions. Since the Love-current solutions have in general a larger energy content than unconstraint solutions, in particular for Huygens surfaces of complicated shape, we would even expect disadvantages due to stronger cancellation effects of the radiated fields. Overall, the achieved accuracy of the fields computed from the obtained sources depends more on the particular problem configuration and the solver stopping criterion than on the choice of sources and/or side constraint, except of course for single-current solutions, which show in general a worse behavior. With respect to the stopping criterion, it is, however, observed that an additional side constraint with a corresponding weighting factor can influence the stopping criterion considerably dependent on the weighting factor and, thus, the results may become less predictable. If one wants to remove the null-space of the IESSP, this can easily be done by a simple combined-source condition, either in strong or in weak form. Finally, it is recommended that the iterative solution of the IESSP is stopped when the achievable OE due to noise and inaccuracies is reached within a reasonable tolerance level, in order to avoid the accumulation of numerical errors. In this respect, the solution of NE systems of equations has a clear advantage compared to the solution of corresponding NR systems of normal equations.

ACKNOWLEDGMENT

This work was supported by the German Research Foundation (DFG) and the Technical University of Munich within the funding programme Open Access Publishing.

APPENDIX A. SURFACE EQUIVALENCE PRINCIPLE REVIEW

Consider a distribution of some material and of radiation sources, e.g., impressed electric and magnetic currents $\mathbf{J}$ and $\mathbf{M}$, inside a volume V enclosed by a surface A with an outward pointing unit normal $\hat{n}$, as for instance seen in Fig. 1. The fields generated by these sources are denoted as $\mathbf{E}_{ext}$ and $\mathbf{H}_{ext}$ for the exterior fields and as $\mathbf{E}_{int}$ and $\mathbf{H}_{int}$ for the interior fields. Without loss of generality, we assume V to be embedded in free space.

The generally accepted form of the equivalence principle states that the exterior fields due to the sources $\mathbf{J}$ and $\mathbf{M}$ in the volume V can be represented by equivalent surface current densities [39, 40, 50–52]

$$\mathbf{J}_A^L = \hat{n} \times \mathbf{H}_{ext}, \qquad \mathbf{M}_A^L = \mathbf{E}_{ext} \times \hat{n} \tag{A1}$$

which are known as Love surface current densties. The interior fields due to these surface current densties are zero. Also, it is clear that the original sources $\mathbf{J}$ and $\mathbf{M}$ are not present anymore after the equivalent surface current densities have been introduced. Since the volume V is now free of any field, its material properties can be changed and it is possible to set up an equivalent free-space problem in order to arrive at equivalent surface current densities radiating in infinite free space.

If we define and solve an interior field problem for the volume V with prescribed tangential electric or magnetic fields on the surface A, and represent the interior fields by corresponding Love equivalent

surface current densities[+], then it is clear that these surface current densities are non-radiating with respect to the exterior of the volume V.

Superimposing the non-radiating surface current densities related to interior fields in V with the equivalent surface current densities in Equation (A1) of the exterior problem, we can construct infinitely many equivalent surface current distributions, which still correctly represent the exterior fields. By choosing

$$\mathbf{E}_{int} \times \hat{n} = \mathbf{E}_{ext} \times \hat{n} \tag{A2}$$

an equivalent surface current distribution with electric surface current densities only will result (see, e.g., also [10]), and with

$$\mathbf{H}_{int} \times \hat{n} = \mathbf{H}_{ext} \times \hat{n}, \tag{A3}$$

an equivalent exterior field representation with magnetic surface current densities only will result.

REFERENCES

1. Parini, C., S. F. Gregson, J. McCormick, and D. J. V. Rensburg, *Theory and Practice of Modern Antenna Range Measurements*, The Institution of Engineering and Technology, London, UK, 2014.
2. Petre, P. and T. Sarkar, "Planar near-field to far-field transformation using an equivalent magnetic current approach," *IEEE Transactions on Antennas and Propagation*, Vol. 40, No. 11, 1348–1356, Nov. 1992.
3. Petre, P. and T. K. Sarkar, "Planar near-field to far-field transformation using an array of dipole probes," *IEEE Transactions on Antennas and Propagation*, Vol. 42, No. 04, 534–537, Apr. 1994.
4. Alvarez, Y., F. Las-Heras, and M. R. Pino, "Reconstruction of equivalent currents distribution over arbitrary three-dimensional surfaces based on integral equation algorithms," *IEEE Transactions on Antennas and Propagation*, Vol. 55, No. 12, 3460–3468, 2007.
5. Quijano, J. L. A. and G. Vecchi, "Field and source equivalence in source reconstruction on 3D surfaces," *Progress In Electromagnetics Research*, Vol. 103, 67–100, 2010.
6. Quijano, J. L. A. and G. Vecchi, "Near- and very near-field accuracy in 3-D source reconstruction," *IEEE Antennas and Wireless Propagation Letters*, Vol. 9, 634–637, 2010.
7. Jorgensen, E., P. Meincke, and C. Cappellin, "Advanced processing of measured fields using field reconstruction techniques," *European Conference on Antennas and Propagation*, Rome, Italy, 2011.
8. Jorgensen, E., D. W. Hess, P. Meincke, O. Borries, and C. Cappellin, "Antenna diagnostics on planar arrays using a 3D source reconstruction technique and spherical near-field measurements," *European Conference on Antennas and Propagation*, Prague, Tzech Republic, 2012.
9. Kilic, E. and T. F. Eibert, "Solution of 3D inverse scattering problems by combined inverse equivalent current and finite element methods," *Journal of Computational Physics*, Vol. 288, 131–149, 2015.
10. Martini, E., G. Carli, and S. Maci, "An equivalence theorem based on the use of electric currents radiating in free space," *IEEE Antennas and Wireless Propagation Letters*, Vol. 7, 421–424, 2008.
11. Eibert, T. F., D. Vojvodic, and T. B. Hansen, "Fast inverse equivalent source solutions with directive sources," *IEEE Transactions on Antennas and Propagation*, Vol. 64, 4713–4724, Nov. 2016.
12. Eibert, T. F. and T. B. Hansen, "Inverse-source algorithm for antenna-field transformations using the weak form of the combined-source condition," *European Conference on Antennas and Propagation*, Paris, France, 2017.
13. Persson, K., M. Gustafsson, and G. Kristensson, "Reconstruction of equivalent currents using a near-field data transformation — with radome applications," *Progress In Electromagnetics Research*, Vol. 54, 179–198, 2005.

[+] Such interior problem solutions can be obtained for arbitrary material property distributions within V. In particular, we are interested in the free-space case. For the solution of the interior field problem, it is convenient to assume at least arbitrarily small losses in order to arrive at a unique field solution with just prescribing the tangential electric or the tangential magnetic fields, respectively.

14. Persson, K., M. Gustafsson, and G. Kristensson, "Reconstruction and visualization of equivalent currents on a radome using an integral representation formulation," *Progress In Electromagnetics Research B*, Vol. 20, 65–90, 2010.
15. Persson, K., M. Gustafsson, G. Kristensson, and B. Widenberg, "Radome diagnostics — source reconstruction of phase objects with an equivalent currents approach," *IEEE Transactions on Antennas and Propagation*, Vol. 62, No. 4, 2041–2051, Apr. 204.
16. Farouq, M., M. Serhir, and D. Picard, "Matrix method for far-field calculation using irregular near-field samples for cylindrical and spherical scanning surfaces," *Progress In Electromagnetics Research B*, Vol. 63, 35–48, 2015.
17. Farouq, M., M. Serhir, and D. Picard, "Antenna far-field assessment from near-field measured over arbitrary surfaces," *IEEE Transactions on Antennas and Propagation*, Vol. 64, No. 12, 5122–5130, 2016.
18. Saad, Y., *Iterative Methods for Sparse Linear Systems*, 2nd Edition, Society for Industrial and Applied Mathematics, 2003.
19. Sarkar, T. and A. Taaghol, "Near-field to near/far-field transformation for arbitrary near-field geometry utilizing an equivalent electric current and MoM," *IEEE Transactions on Antennas and Propagation*, Vol. 47, No. 3, 1178–1185, 1999.
20. Eibert, T. F. and C. H. Schmidt, "Multilevel fast multipole accelerated inverse equivalent current method employing Rao-Wilton-Glisson discretization of electric and magnetic surface currents," *IEEE Transactions on Antennas and Propagation*, Vol. 57, No. 4, 1178–1185, 2009.
21. Eibert, T. F., Ismatullah, E. Kaliyaperumal, and C. H. Schmidt, "Inverse equivalent surface current method with hierarchical higher order basis functions, full probe correction and multilevel fast multipole acceleration (invited paper)," *Progress In Electromagnetics Research*, Vol. 106, 377–394, 2010.
22. Eibert, T. F., E. Kilic, C. Lopez, R. A. Mauermayer, O. Neitz, and G. Schnattinger, "Electromagnetic field transformations for measurements and simulations (invited paper)," *Progress In Electromagnetics Research*, Vol. 151, 127–150, 2015.
23. Alvarez, Y., F. Las-Heras, and M. R. Pino, "Acceleration of the sources reconstruction method via the fast multipole method," *IEEE Antennas and Propagation International Symposium*, San Diego, CA, USA, 2008.
24. Foged, L. J., L. Scialacqua, F. Saccardi, J. L. A. Quijano, and G. Vecchi, "Application of the dual-equation equivalent-current reconstruction to electrically large structures by fast multipole method enhancement," *IEEE Antennas and Propagation Magazine*, Vol. 56, No. 5, 264–273, 2014.
25. Coifman, R., V. Rokhlin, and S. Wandzura, "The fast multipole method for the wave equation: A pedestrian prescription," *IEEE Antennas and Propagation Magazine*, Vol. 35, No. 3, 7–12, 1993.
26. Chew, W. C., J.-M. Jin, E. Michielssen, and J. Song, *Fast and Efficient Algorithms in Computational Electromagnetics*, Artech House, Boston, 2001.
27. Eibert, T. F., "A diagonalized multilevel fast multipole method with spherical harmonics expansion of the k-space integrals," *IEEE Transactions on Antennas and Propagation*, Vol. 53, No. 2, 814–817, 2005.
28. Lopez, Y. A., M. R. Pino, and F. Las-Heras, "Application of the adaptive cross approximation algorithm to the sources reconstruction method," *European Conference on Antennas and Propagation*, Berlin, Germany, 2009.
29. Wang, Y., T. F. Eibert, and Z. Nie, "Adaptive cross approximation algorithm accelerated inverse equivalent current method for near-field antenna measurement," *IEEE Transactions on Antennas and Propagation*, Vol. 67, No. 3, 1874–1883, Mar. 2019.
30. Zhao, K., M. N. Vouvakis, and J.-F. Lee, "The adaptive cross approximation algorithm for accelerated method of moments computations of EMC problems," *IEEE Transactions on Electromagnetic Compatibility*, Vol. 47, No. 4, 763–773, 2005.
31. Hansen, T. B., A. Paulus, and T. F. Eibert, "On the condition number of a normal matrix in near-field to far-field transformations," *IEEE Transactions on Antennas and Propagation*, Vol. 67, 2028–2033, Mar. 2019.

32. Hsiao, G. C. and R. E. Kleinman, "Mathematical foundations for error estimation in numerical solutions of integral equations in electromagnetics," *IEEE Transactions on Antennas and Propagation*, Vol. 45, No. 3, 316–328, Mar. 1997.
33. Kornprobst, J., R. A. M. Mauermayer, E. Kilic, and T. F. Eibert, "An inverse equivalent surface current solver with zero-field enforcement by left-hand side Calderón projection," *European Conference on Antennas and Propagation*, 1–4, Krakau, Polen, 2019.
34. Kong, J. A., *Electromagnetic Wave Theory*, 2nd Ed., John Wiley & Sons, New York, 1990.
35. Mauermayer, R. A. M. and T. F. Eibert, "Fast irregular antenna field transformation above perfectly conducting ground planes," *European Conference on Antennas and Propagation (EUCAP)*, Davos, Switzerland, 2016.
36. Eibert, T. F. and R. A. M. Mauermayer, "Near-field far-field transformations for automobile antenna measurements," *Applied Computational Electromagnetics Society Conference*, Denver, CO, USA, 2018.
37. Eibert, T. F. and R. A. M. Mauermayer, "Equivalent sources based near-field far-field transformation above dielectric half space," *Annual Symposium of the Antenna Measurement Techniques Association (AMTA)*, Williamsburg, VA, USA, 2018.
38. Neitz, O., R. A. M. Mauermayer, Y. Weitsch, and T. F. Eibert, "A propagating plane-wave based near-field transmission equation for antenna gain determination from irregular measurement samples," *IEEE Transactions on Antennas and Propagation*, Vol. 65, No. 8, 4230–4238, Aug. 2017.
39. Love, A. E. H., "The integration of the equations of propagation of electric waves," *Philosophical Transactions of the Royal Society A*, Vol. 197, No. 287–289, 1–43, 1901.
40. Schelkunoff, S., "Some equivalence theorems of electromagnetics and their application to radiation problems," *Bell System Technical Journal*, Vol. 15, No. 1, 92–112, 1936.
41. Peterson, A. F., S. L. Ray, and R. Mittra, *Computational Methods for Electromagnetics*, Wiley-IEEE Press, 1997.
42. Mautz, J. R. and R. F. Harrington, "A combined-source solution for radiation and scattering from a perfectly conducting body," *IEEE Transactions on Antennas and Propagation*, Vol. 27, No. 4, 445–454, Jul. 1979.
43. Rao, S. M., D. R. Wilton, and A. W. Glisson, "Electromagnetic scattering by surfaces of arbitrary shape," *IEEE Transactions on Antennas and Propagation*, Vol. 30, No. 1, 409–418, 1982.
44. Kornprobst, J. and T. F. Eibert, "An accurate low-order discretization scheme for the identity operator in the magnetic field and combined field integral equations," *IEEE Transactions on Antennas and Propagation*, Vol. 66, 6146–6157, Nov. 2018.
45. Eibert, T. F. and D. Vojvodić, "Fast inverse equivalent current solutions with surface currents in complex space," *URSI Electromagnetic Theory Symposium*, Espoo, Finland, 2016.
46. Hansen, T. B., "Translation operator based on Gaussian beams for the fast multipole method in three dimensions," *Wave Motion*, Vol. 50, No. 5, 940–954, 2013.
47. Altair, FEKO, 2019, [Online], Available: https://altairhyperworks.com/product/FEKO.
48. NSI-MI, Microwave test systems, 2019, [Online], Available: https://www.nsi-mi.com/.
49. Rohde & Schwarz, HF907, 2019, double-ridged waveguide antenna.
50. Jin, J.-M., *Theory and Computation of Electromagnetic Fields*, John Wiley & Sons, Inc., New York, 2015.
51. Rengarajan, S. R. and Y. Rahmat-Samii, "The field equivalence principle: Illustration of the establishment of the non-intuitive null fields," *IEEE Antennas and Propagation Magazine*, Vol. 42, No. 4, 122–128, 2000.
52. Yaghjian, A. D., "Three-dimensional planar surface-current equivalence theorem with application to receiving antennas as linear differential operators," *Radio Science*, Vol. 37, No. 2, VIC 4–1–VIC 4–10, 2002.